

# Toward Enhancing Desalination and Heavy Metal Removal of TFC Nanofiltration Membranes: A Cost-Effective Interface Temperature-Regulated Interfacial Polymerization

Xiaoxiang Cheng, Cunxian Lai, Jinyu Li, Weiwei Zhou, Xuewu Zhu,\* Zihui Wang, Junwen Ding, Xinyu Zhang, Daoji Wu, Heng Liang, and Congcong Zhao



Cite This: <https://doi.org/10.1021/acsami.1c17783>



Read Online

ACCESS |



Metrics & More



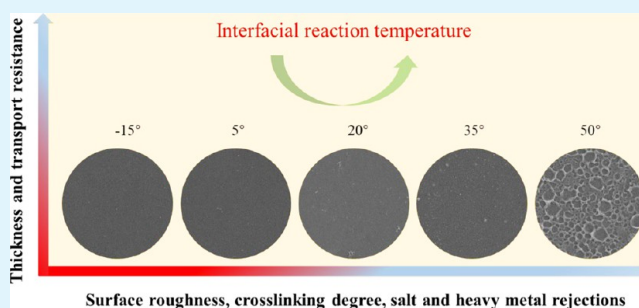
Article Recommendations



Supporting Information

**ABSTRACT:** Polyamide (PA) chemistry-based nanofiltration (NF) membranes have an important role in the field of seawater desalination and wastewater reclamation. Achieving an ultrathin and defect-free active layer via precisely controlled interfacial polymerization (IP) is an effective routine to improve the separation efficiencies of NF membranes. Herein, the morphologies and chemical structures of the thin-film composite (TFC) NF membranes were accurately regulated by tailoring the interfacial reaction temperature during the IP process. This strategy was achieved by controlling the temperature ( $-15$ ,  $5$ ,  $20$ ,  $35$ , and  $50^\circ$ ) of the oil-phase solutions. The structural compositions, morphological variations, and separation features of the fabricated NF membranes were studied in detail. In addition, the formation mechanisms of the NF membranes featuring different PAs were also proposed and discussed. The temperature-assisted IP (TAIP) method greatly changed the compositions of the resultant PA membranes. A very smooth and thin PA film was obtained for the NF membranes fabricated at a low interfacial temperature; thus, a high  $19.2 \text{ L m}^{-2} \text{ h}^{-1} \text{ bar}^{-1}$  of water permeance and 97.7% of  $\text{Na}_2\text{SO}_4$  rejection were observed. With regard to the NF membranes obtained at a high interfacial temperature, a lower water permeance and higher salt rejection with fewer membrane defects were achieved. Impressively, the high interfacial temperature-assisted NF membranes exhibited uniform coffee-ring-like surface morphologies. The special surface-featured NF membrane showed superior separation for selected heavy metals. Rejections of 93.9%, 97.9%, and 87.7% for  $\text{Cu}^{2+}$ ,  $\text{Mn}^{2+}$ , and  $\text{Cd}^{2+}$  were observed with the optimized membrane. Three cycles of fouling tests indicated that NF membranes fabricated at low temperatures exhibited excellent antifouling behavior, whereas a high interface temperature contributed to the formation of NF membranes with high fouling tendency. This study provides an economical, facile, and universal TAIP strategy for tailoring the performances of TFC PA membranes for environmental water treatment.

**KEYWORDS:** polyamide, nanofiltration membranes, temperature-assisted interfacial polymerization (TAIP), thin-film composite (TFC), heavy metals



## 1. INTRODUCTION

In the coming decades, water pollution and a shortage of fresh water will become the main issues troubling human existence. Wastewater recycling and brackish water desalination can provide people with a steady supply of clean water.<sup>1–5</sup> As a typical purification process between ultrafiltration and reverse osmosis, nanofiltration (NF) membranes can effectively reject small molecules and divalent ions with molecular weights above 200 Da.<sup>6,7</sup> Owing to their unique separation behavior, NF membranes are already increasingly applied in environmental water treatment processes.<sup>8</sup> Among the commercially available NF membranes, polyamide (PA)-based composite NF membranes possessing a thin separation layer over an ultrafiltration support are the most popular ones because of their production feasibility and excellent separation perform-

ance.<sup>9–12</sup> Despite the fact that the support membranes greatly affect the generation of the top PA film,<sup>13</sup> the natural features of the top PA film dominate the separation ability of the composite membrane. Therefore, precise regulation of the selective PA layer can be promising in expanding their applications.

The PA layer of the composite NF membrane is generally fabricated via the interfacial polymerization (IP) reaction

**Received:** September 15, 2021

**Accepted:** November 12, 2021



**Figure 1.** Schematic presentation for fabricating TFC NF membranes via the TAIP method.

between piperazine (PIP) and trimesoyl chloride (TMC) near the water/oil interface.<sup>14</sup> Once the aqueous- and oil-phase monomers contact at the incompatible interface, the IP reaction occurs immediately and a dense cross-linked film is formed.<sup>15</sup> Owing to the generation of the PA film, further diffusion of the aqueous phase across the nascent membrane is strictly hindered. This phenomenon is also called the “self-sealing” effect of the IP reaction process.<sup>16</sup> Consequently, a much thinner separation layer is achieved compared to that of the symmetrically structured NF membranes fabricated by the phase inversion method.<sup>17</sup> Benefiting from the special formation mechanisms of the IP-based TFC NF membranes, the accurate control of the transfer rate of the PIP monomers into the organic solutions is assumed to be an efficient method to regulate the generation of a PA film with tailored structure and performance.<sup>18</sup>

To date, various approaches have been adopted to control the diffusion rate of the PIP monomers, thus tailoring the performance of the TFC NF membranes. Numerous studies have reported that modification of the supports could increase the surface porosity and hydrophilicity,<sup>19–21</sup> thus leading to higher adsorption of PIP monomers. The abundant PIP monomers contribute to a faster IP reaction rate, resulting in the generation of an ultrathin PA film featuring higher water permeance. Though better performance is achieved for the resultant NF membranes, the modification of the support membrane is always time consuming and complicated. Creating interlayers between the support and the top PA layer provides an alternative approach for regulating the diffusion rate of the PIP monomers, thereby constructing high-performance NF membranes without functionalizing the supports.<sup>22–25</sup> The highly efficient NF membranes have successfully broken the trade-off lines for TFC desalination membranes, but the compatibility of the triple layers is far from satisfactory. In situ incorporation of macromolecules/inorganic salts into the aqueous solutions was considered as an efficient and scalable strategy to confine the diffusion of PIP monomers via hydrogen bonding, reactive complexation, and electrostatic interaction.<sup>26–29</sup> However, previous studies mainly focus on the PIP diffusion regulation; the tailored diffusion of TMC and the simultaneous diffusion control of both the PIP and TMC monomers have rarely been reported. Considering the differences in the transport behavior during the IP reaction, it is of great value to explore the role of the simultaneous

confined diffusion for the PIP and TMC monomers in the structure and performance of the TFC NF membranes.

As the IP reaction happens near the organic-phase side, the diffusion of PIP monomers in the organic solution dominates the formation of the PA film. Decreasing the temperature of the organic solvent allows the increase in surface tension and viscosity, thus leading to a lower diffusivity into the organic phase.<sup>30</sup> Meanwhile, the reduced temperature will also lead to a slower transfer rate of TMC toward the reaction interface. Therefore, decreasing the temperature of the organic phase during IP can simultaneously confine the diffusion rate of the PIP and TMC monomers. Inspired by this, we proposed a cost-effective temperature-assisted IP (TAIP) strategy for regulating the IP reaction rate for TFC NF membranes, thus tailoring the morphology and separation performance. The interface reaction temperature was accurately controlled by changing the temperature of the oil-phase monomers. The temperature-induced variations of the morphological features, structural compositions, and separation characters for the NF membranes were systematically evaluated. In addition, the rejections for typical heavy metals were also performed. The TAIP strategy contributed to the construction of NF membranes with different separation performance owing to various surface morphologies. Therefore, this study provides an economical and effective way of fabricating performance-tailored TFC NF membranes.

## 2. EXPERIMENTAL SECTION

**2.1. Chemicals and Materials.** Piperazine (PIP,  $\geq 99.9\%$ ), isopropyl alcohol (IPA,  $\geq 99.5\%$ ), bovine serum albumin (BSA,  $\geq 99.0\%$ ), and sodium hydroxide (NaOH,  $\geq 99.5\%$ ) were purchased from Macklin (Shanghai, China). Manganese chloride ( $\text{MnCl}_2$ ,  $99.0\%$ ), magnesium sulfate ( $\text{MgSO}_4$ ,  $\geq 99.0\%$ ), sodium sulfate ( $\text{Na}_2\text{SO}_4$ ,  $\geq 99.0\%$ ), chloroform ( $\text{CHCl}_3$ ,  $99.0\%$ ), calcium chloride ( $\text{CaCl}_2$ ,  $\geq 99.0\%$ ), sodium bicarbonate ( $\text{NaHCO}_3$ ,  $\geq 99.0\%$ ), sodium chloride ( $\text{NaCl}$ ,  $\geq 99.5\%$ ), cadmium chloride ( $\text{CdCl}_2$ ,  $\geq 99.0\%$ ), magnesium chloride ( $\text{MgCl}_2$ ,  $\geq 99.0\%$ ), and copper chloride ( $\text{CuCl}_2$ ,  $\geq 98.0\%$ ) were provided by Aladdin Chemical Reagent Co., Ltd. (Shanghai, China). Polyethylene glycols of various molecular weights (PEGs,  $M_w = 200, 400, 600, 800, \text{ and } 1000 \text{ g mol}^{-1}$ ) and 1,3,5-benzenetricarbonyl trichloride (TMC,  $\geq 98.0\%$ ) were purchased from TCI Chemicals (Tokyo, Japan). Unless otherwise stated, all reagents were dissolved in deionized water provided by an ultrapure water system (Milli-Q IQ7005, USA). The poly(ether sulfone) (PES-150) ultrafiltration support with a pore size of  $\sim 150 \text{ kDa}$  was bought from Microdyn-Nadir Xiamen Co., Ltd. (Xiamen, China). A commercial

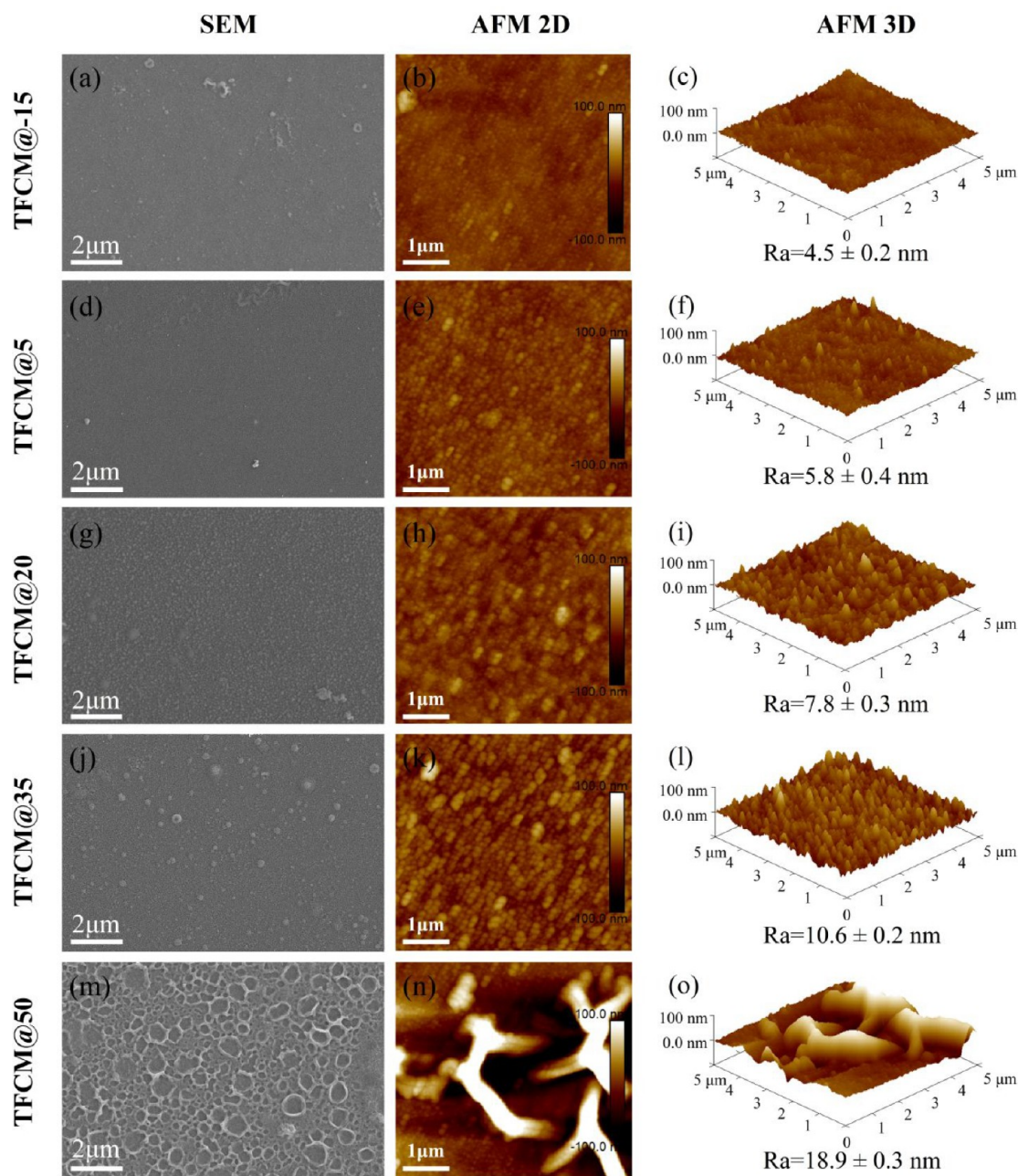


**Figure 2.** Morphological characterizations of the fabricated NF membranes: SEM and AFM (2D, 3D) images of (a–c) TFCM@–15, (d–f) TFCM@5, (g–i) TFCM@20, (j–l) TFCM@35, and (m–o) TFCM@50.

NF270 membrane provided by Dow was used for performance comparisons.

**2.2. Fabrication of the NF Membranes.** The TFC NF membranes were prepared by a modified IP process, as shown in Figure 1. First, the PES ultrafiltration membrane was clipped into pieces with an active area of 44.0 cm<sup>2</sup> using a circular cutter. Second, the tailored membrane samples were immersed into a 30 wt % IPA solution for 10 min to remove any residual chemical agents on the surface. Third, the support membranes were cleaned with pure water 3 times to thoroughly remove the extra IPA residual. The pretreated PES support was then fixed in a circular organic glass reactor with its separation layer facing up. After membrane fixing, 15 mL of an aqueous solution containing 1.0 wt % PIP and 0.5 wt % NaOH at 20 °C was poured into the reactor and soaked for 2 min. After the adsorption procedure of the PIP monomers, the extra solution was poured away, and the membrane surface was dried with an air knife until no obvious water droplet was seen. The distance between the

membrane surface and the air knife was controlled at 10–15 cm, the air velocity was set at 20 L min<sup>–1</sup>, and the total gassing time was kept at 1 min. When the membrane drying process was completed, a 0.1 wt % TMC/hexane solution with various temperatures (from –15 to 50 °C) was again poured into the reactor and stood for 30 s. After pouring the excess solution, the resultant membrane was put into a 60 °C water bath for 5 min to complete the heat-curing process. Lastly, the final NF membrane with a cross-linked structure (Figure S1) was stored in ultrapure water at 5 °C. On the basis of the differences in the interfacial temperature during the IP process, the fabricated NF membranes were marked as TFCM@–15, TFCM@5, TFCM@20, TFCM@35, and TFCM@50.

**2.3. Characterizations of the NF Membranes.** The chemical structures and element contents of the membrane surfaces were characterized by attenuated total reflection Fourier transform infrared spectrometry (ATR-FTIR,ENSOR, Bruker) with a scanning wavelength of 500–4000 cm<sup>–1</sup> and X-ray photoelectron spectroscopy (XPS, Phi

Quanter II, ULVAC-Phi), respectively. The mean roughness ( $R_a$ ) of the films was measured by atomic force microscopy (AFM, Dimension Icon, Bruker) with a scanning zone of  $5 \mu\text{m} \times 5 \mu\text{m}$ . The surface morphologies and cross-sectional features of the membranes were measured by field emission scanning electron microscopy (SEM, Sigma 300, ZEISS) and transmission electron microscopy (TEM, Talos F200S, Thermo Scientific), respectively. The dynamic potential and contact angle measurement provided by the solid surface zeta potential analyzer (Surpass3, Anton Paar) and the contact angle measurement instrument (DSA25, Kruss) were used to analyze the charge characteristics and surface hydrophilicity of the membrane surfaces. During the tests, at least 3 parallel experiments were conducted for each membrane type.

**2.4. Separation Performance Evaluations of the NF Membranes.** The filtration performance of the NF membranes was measured by a self-assembled dead-end filtration system, as shown in Figure S2. To reduce concentration polarization during the rejection tests, the stirring rate of the filtration cell was set as  $300 \text{ r min}^{-1}$ . During the test, the temperature and filtration pressure were controlled at  $25.0 \pm 0.2 \text{ }^\circ\text{C}$  and  $0.4 \text{ MPa}$ , respectively. Prior to the filtration tests, the NF films were prestabilized at  $0.6 \text{ MPa}$  for 24 h. Ultrapure water was used to evaluate the permeability, whereas 2000 ppm of four typical ionic salts ( $\text{NaCl}$ ,  $\text{MgCl}_2$ ,  $\text{MgSO}_4$ , and  $\text{Na}_2\text{SO}_4$ ) and 100 ppm of heavy metals ( $\text{MnCl}_2$ ,  $\text{CuCl}_2$ , and  $\text{CdCl}_2$ ) were applied to study the separation properties of the NF membranes. In addition, 200 ppm of PEGs ( $200\text{--}1000 \text{ g mol}^{-1}$ ) was utilized to calculate the pore diameter of the NF membranes. A conductivity meter (DDS-307A, INESA, China), an atomic absorption spectrometer (AAS, iCE 300, Thermo Scientific, USA), and a total organic carbon meter (TOC-L SHIMADZU, Tokyo) were used to measure the contents of the salts and PEGs in the feed and permeate, respectively. The water permeance ( $J$ ,  $\text{L m}^{-2} \text{ h}^{-1} \text{ bar}^{-1}$ ), salt rejections ( $R$ , %), and separation selectivity ( $\alpha$ ) of  $\text{NaCl}$  to  $\text{Na}_2\text{SO}_4$  can be calculated by the following equations<sup>31–33</sup>

$$J = \frac{V}{AtP} \quad (1)$$

$$R = \left(1 - \frac{C_p}{C_f}\right) \times 100\% \quad (2)$$

$$\alpha = \frac{(C_{\text{NaCl}}/C_{\text{Na}_2\text{SO}_4})_p}{(C_{\text{NaCl}}/C_{\text{Na}_2\text{SO}_4})_f} = \frac{1 - R_{\text{NaCl}}}{1 - R_{\text{Na}_2\text{SO}_4}} \quad (3)$$

where  $V$  represents the filtration volume (L),  $A$  is the effective membrane area ( $\text{m}^2$ ),  $t$  stands for the filtration time (h),  $P$  is the operating pressure (bar), and  $C_p$  and  $C_f$  ( $\mu\text{S cm}^{-1}$  or  $\text{mg L}^{-1}$ ) are the solute contents in the permeate and feed, respectively.

The mean pore size ( $\mu_p$ , nm) and geometric standard deviation ( $\sigma$ ) of the NF membranes can be obtained by the PEG rejections, as expressed in eqs 4 and 5<sup>34–36</sup>

$$d_s = 33.46 \times 10^{-3} \times M^{0.577} \quad (4)$$

$$\frac{dR(d_p)}{dd_p} = \frac{1}{d_p \ln \sigma_p \sqrt{2\pi}} \exp\left[-\frac{(\ln d_p - \ln \mu_p)^2}{2(\ln \sigma_p)^2}\right] \quad (5)$$

**2.5. Antifouling Behavior and Stability of the NF Membranes.** To ensure the same hydrodynamic conditions, a consistent initial water flux of  $35.0 \text{ L m}^{-2} \text{ h}^{-1}$  was applied during the fouling tests via adjusting the operation pressure. The antifouling experiment was evaluated by employing BSA as the model foulant using the following steps: First, ultrapure water was filtrated until a steady water flux ( $J_0$ ) was obtained. Then, a feed solution composed of 100 ppm of BSA and background electrolyte (16 mM  $\text{NaCl}$ , 1 mM  $\text{NaHCO}_3$ , and 1 mM  $\text{CaCl}_2$ ) was added into the filtration cell. During the foulant filtration process, the time-dependent water flux ( $J_{w,t}$ ) was monitored by the online data transmission system. Third, ultrapure water cleaning was conducted for 1 h to remove the deposited foulant and recover the water flux ( $J_r$ ) of the NF membranes. This procedure

was repeated for 3 cycles for a better understanding of the long-term antifouling behavior of the NF membranes. The stirring rate and temperature of the cell were maintained at  $300 \text{ r min}^{-1}$  and  $25.0 \pm 0.2 \text{ }^\circ\text{C}$ . To evaluate the fouling reversibility, the flux decay ratio (FDR) and flux recovery ratio (FRR) were calculated as follows.<sup>37</sup> A 40 h filtration using 2000 ppm of  $\text{Na}_2\text{SO}_4$  solution was performed to estimate the long-term stability of the NF membranes. During the filtration process, the water permeance and  $\text{Na}_2\text{SO}_4$  rejection were measured periodically.

$$\text{FDR} = \left(1 - \frac{J_{w,t}}{J_0}\right) \times 100 \quad (6)$$

$$\text{FRR} = \frac{J_r}{J_0} \times 100 \quad (7)$$

### 3. RESULTS AND DISCUSSION

**3.1. Surface Morphologies of the NF Membranes.** The surface morphologies of the resultant NF membranes were determined by the SEM and AFM images. As displayed in Figure S3, homogeneous surface pores can be clearly observed on the PES support membrane. Obviously, the surface membrane pores of the substrate became invisible for all of the NF membranes (Figure 2), proving that the IP reaction had been successfully carried out and the newly generated PA layer covered the original pores. For TFCM@-15, a very smooth surface was obtained (Figure 2a), which was totally different from the rough surface features of typical NF membranes fabricated at room temperature.<sup>38</sup> It is widely accepted that the rough surface of the TFC membranes is greatly linked to the interface heat-induced nanobubble releasing during the IP reaction.<sup>39</sup> Cooling the organic solution could effectively neutralize the heat generated by IP, thus inhibiting the release of the nanobubbles existing in the aqueous solution. Increasing the interfacial reaction temperature (IRT) resulted in a gradually rougher membrane surface. For the NF membranes fabricated at an IRT lower than  $20 \text{ }^\circ\text{C}$ , smooth surfaces with almost no special morphological features were observed. The typical nodular-like structures began to appear on the membrane surface for TFCM@20 (Figure 2g), which is consistent with a previous study.<sup>40</sup> These unique nodular structures became more obvious and numerous on the membrane surfaces of TFCM@20 and TFCM@35, as seen in Figure 2g and 2j. Interestingly, coffee-ring-like structured morphologies occurred on the surface of the TFCM@50 (Figure 2m). Similar surface morphologies were also observed in the cross-sectional TEM images of the resultant NF membranes, as displayed in Figure S4. After the IP reaction, a thin PA film could be clearly seen and different morphological features were obtained for the NF membranes with the increased IRT. This special structure is likely ascribed to the high-temperature and organic solution evaporation-induced interface instability and nanobubble-releasing process. As the IP reaction was a heat-releasing process,<sup>41</sup> an increased disturbance of the reaction interface could be achieved by increasing the reaction temperature. Because of the high volatility, the high temperature would promote the evaporation of the organic solution and further increase the interface instability. As a result, the reaction interface became increasingly unstable, leading to the formation of an irregular wrinkle-like morphology. In addition, the increased heat release also accelerated the degassing of the dissolved gases.<sup>42</sup> The released nanobubbles were encapsulated by the

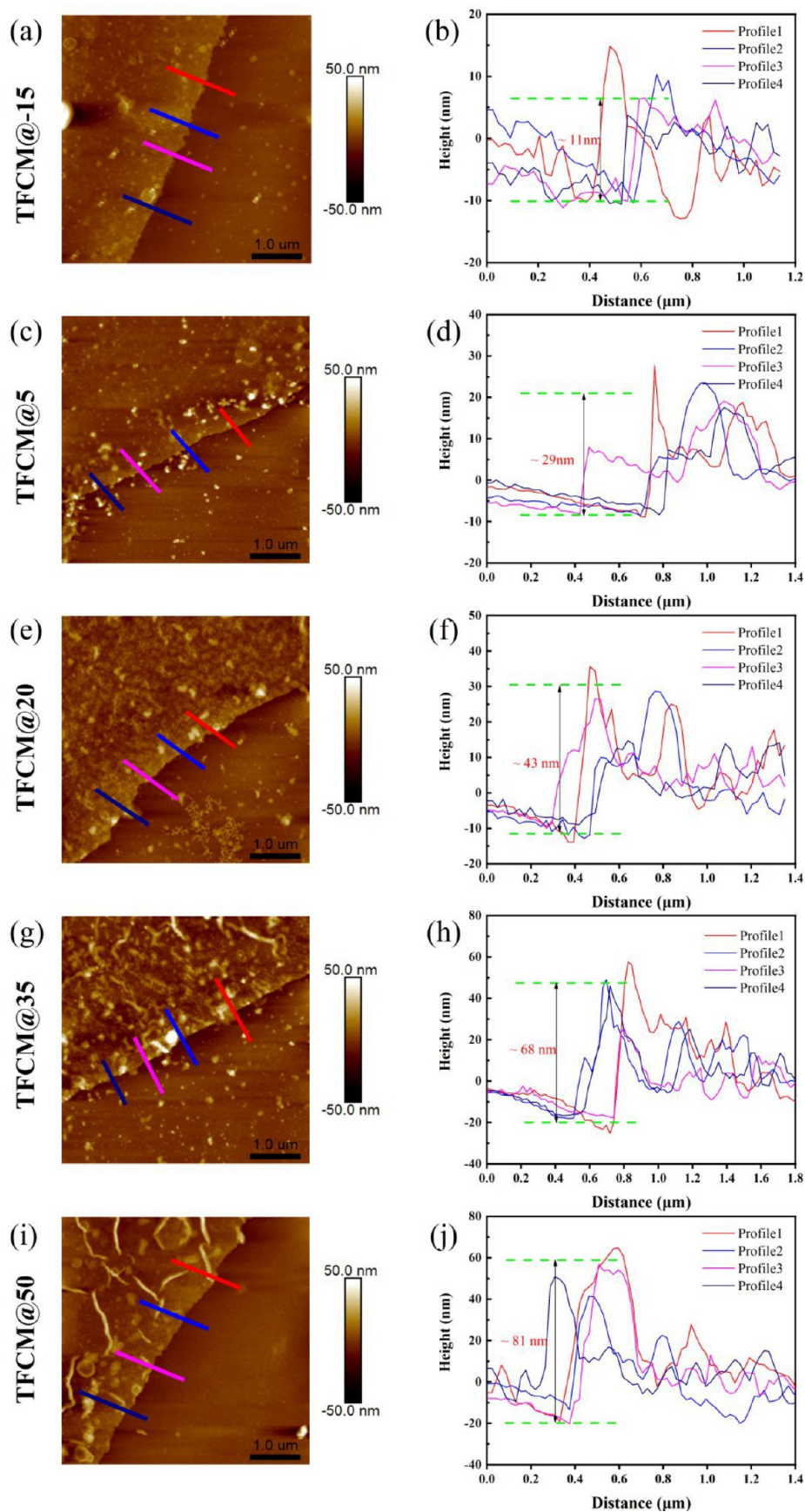


**Figure 3.** AFM-characterized height profiles of the NF membranes: 2D images and height curves of (a, b) TFCM@-15, (c, d) TFCM@5, (e, f) TFCM@20, (g, h) TFCM@35, and (i, j) TFCM@50.

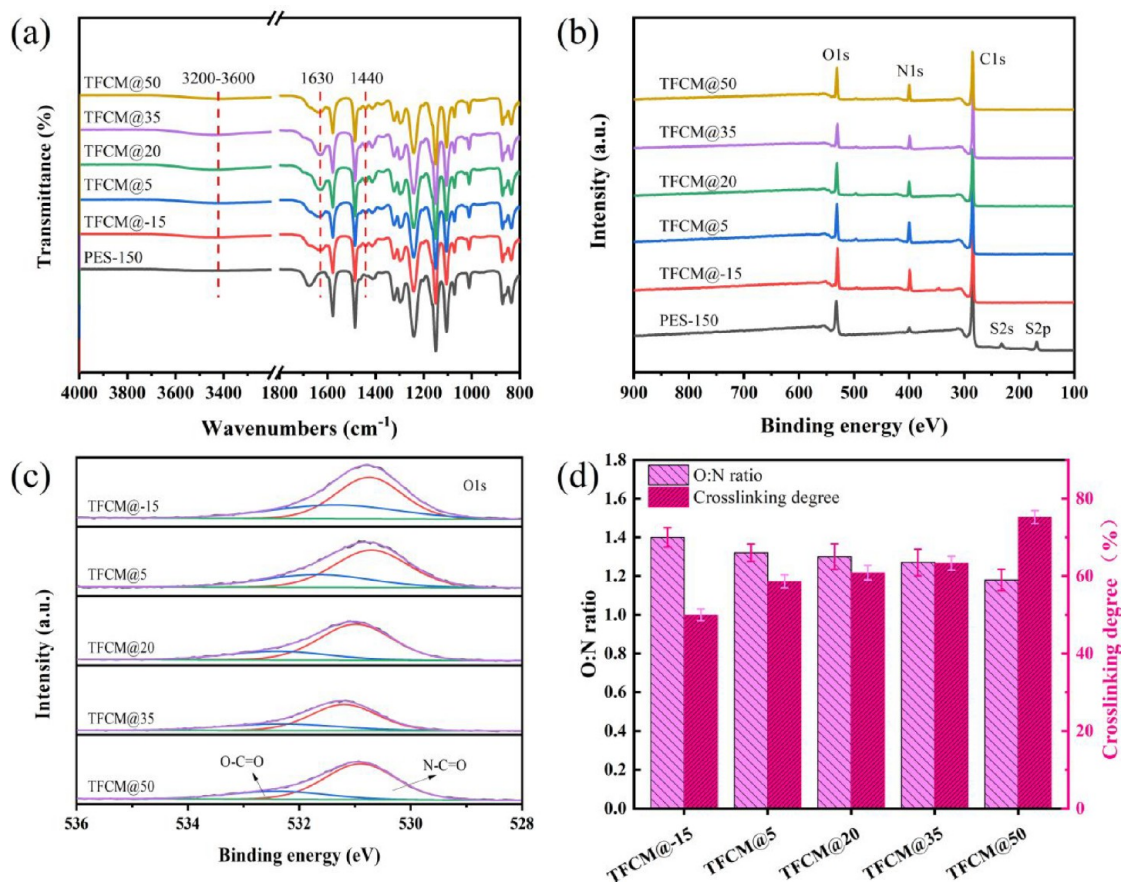


**Figure 4.** Chemical characteristics of the resultant NF membranes: (a) ATR-FTIR, (b) XPS, (c) high-resolution O 1s spectrum, and (d) ratio of O to N and corresponding cross-linking degree (DNC).

quickly generated PA film, contributing to a larger sized nodular. Therefore, both the increased interface instability and the nanobubbles led to the unique coffee-ring-like morphology for TFCM@50. A similar morphological change was observed for the surface roughness of the resultant NF membranes, as depicted in the AFM 2D and 3D images. As seen, increased surface roughness was achieved when increasing the interface temperature. The TFCM@-15 membrane showed a very smooth surface, exhibiting a  $R_a$  of  $2.5 \pm 0.2$  nm. With the interface temperature increasing from 5 to 50 °C, the  $R_a$  value increased from  $5.8 \pm 0.2$  nm for TFCM@5 to  $18.9 \pm 0.3$  nm for TFCM@50. Obviously, the roughest surface belonged to the TFCM@50 membrane, which could be explained by the newly formed coffee-ring-like morphologies.

The PA layer thickness of the NF membranes was further analyzed by AFM height measurement. Before the tests, the NF membranes were prewetted and pasted on the silicon wafer with their active layers up. After that, the silicon wafer was immersed into pure chloroform solutions to completely dissolve the PES support.<sup>43</sup> The thickness of the PA film was measured by analyzing the differences between the film and the silicon wafer, as shown in Figure 3. For the TFCM@-15 membrane, the thinnest height was observed with a thickness of  $\sim 11$  nm (Figure 3b). On increasing the interface temperature, the height of the PA layer gradually increased. As calculated, the thickness of the PA layer was 29, 43, 68, and 81 nm for TFCM@5, TFCM@20, TFCM@35, and TFCM@50, respectively. The increase in the interface temperature further contributed to the diffusion of the TMC monomers

across the water/oil interface,<sup>44</sup> thus leading to the further IP reaction with PIP and resulting in a thicker PA film. On the contrary, the diffusion rate of PIP in the organic solution was greatly confined due to the higher viscosity and surface tension caused by the reduced solvent temperature. Besides, the transport rate of the TMC monomers toward the reaction interface was much slower at a low temperature than that at a high temperature, leading to a very thin PA layer for the TFCM@-15 membrane. This result demonstrated that the height of the PA film could be tailored by changing the IRT. Tian et al. reported that an ultrathin PA film could be generated by choosing appropriate support and monomer concentrations.<sup>45</sup> Compared with other tailoring methods such as support membrane modification, nanomaterials incorporation, and gutter layer-assisted IP, the IRT regulation during the IP process was much easier to operate and realize in large-scale production without changing the original manufacturing process.

**3.2. Structural Characterization of the NF Membranes.** In order to analyze the chemical structures and elemental compositions of the NF membranes, the surface functional groups and elemental percentages were measured by FTIR and XPS. As seen in Figure 4a, typical peaks for the PA NF membranes appeared at 3200–3600, 1630, and 1440  $\text{cm}^{-1}$ , corresponding to the vibration stretching of O–H, vibration stretching of C=O, and vibration stretching of O–H, respectively.<sup>46–49</sup> These results confirm that the IP reaction was successfully performed at both low and high interface temperatures. The effects of the interface temperature on the

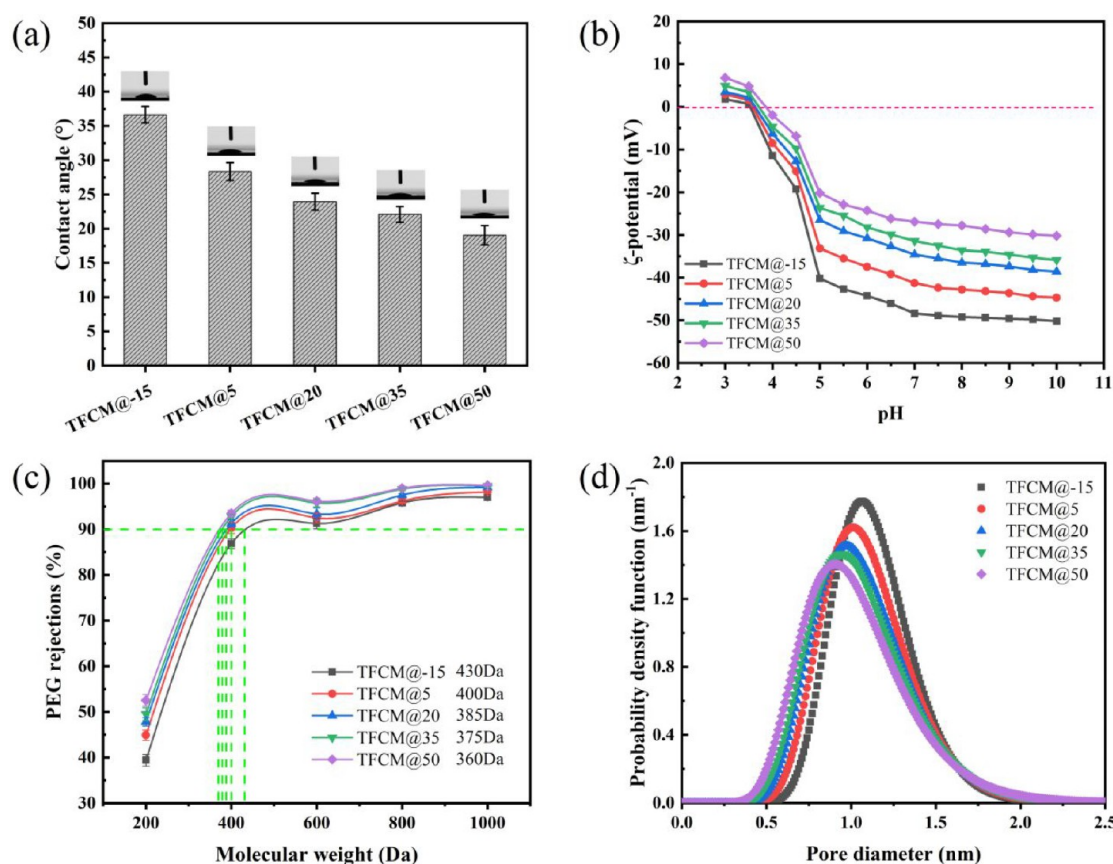


**Figure 5.** (a) Surface hydrophilicity, (b) surface charge, (c) PEG-characterized MWCOs changes, and (d) average pore diameter of the fabricated NF membranes.

elemental compositions of the membrane surfaces for the NF membranes were evaluated by XPS, as compared in Figure 4b. It is observed that the three typical characteristic peaks of C, N, and O for PA film were present in all types of NF membranes. In addition, the typical peak of the S element belonging to the PES support was absent in the spectrum of the NF membranes, demonstrating that no obvious defects were formed via increasing the interfacial temperature.<sup>50</sup> To quantitatively analyze the role of interface temperature in the contents of functional groups on the membrane surface, the characteristic peak of the O 1s element was convoluted into two peaks, O–C=O and N–C=O, respectively (Figure 4c).<sup>51</sup> With increasing interface temperature, the content of the O–C=O groups decreased from 38.8% for TFCM@–15 to 23.6% for TFCM@50. The decreased O–C=O groups indicate that a more cross-linked and defect-free PA film was constructed at a higher interface temperature.<sup>52</sup> This result can be assigned to the accelerated IP reaction rate caused by the temperature-promoted diffusion. At a low temperature, the diffusion rate of the TMC monomers toward the water/oil interface was slow and less TMC could react with PIP, resulting in more TMC monomers unreacted on the membrane surface and then hydrolyzed into O–C=O groups. On the contrary, a high temperature contributed to the fast transport of TMC to the reaction interface and led to a more complete IP reaction with PIP. Consequently, a relatively lower content of TMC could be hydrolyzed; thus, a lower content of O–C=O groups was achieved for TFCM@50. With respect to N-contained groups, a higher content of N–C=O groups was observed for TFCM@50 than that of TFCM@–15 (Figure S5), implying

that more cross-linked structures existed in the formed PA film. Similar to the elemental deconvolution results, the O/N ratio and cross-linking degree (DNC) were further calculated based on the XPS-characterized elemental compositions. As shown in Figure 4d, a gradually decreasing O/N ratio and increasing DNC were obtained with increasing interface temperature. In particular, the O/N ratio decreased from 1.40 for TFCM@–15 to 1.18 for TFCM@50. Correspondingly, the DNC was in the order of TFCM@–15 < TFCM@5 < TFCM@20 < TFCM@35 < TFCM@50. The increase in DNC was in favor of lowering the surface defects for a typical NF membrane, thus enhancing the separation behavior during the filtration tests. Of note, the increased DNC would lead to a narrower pore size as well, which was not beneficial to the improvement of the water permeance for the membranes. To this end, increasing the interface temperature facilitated the formation of a dense PA film with fewer defect-free sites.

**3.3. Membrane Hydrophilicity, Charge, and Pore Size.** The surface hydrophilicity, charge features, and pore sizes of the NF membranes were further estimated by characterizing the pure water contact angles, zeta potentials, and PEG rejections, respectively. Figure 5a illustrates the dynamic water contact angle of the NF membranes. As observed, the average contact angle of all of the membranes was lower than 40°, indicating that the NF membranes had a relatively hydrophilic surface, which is in agreement with typical NF membranes.<sup>53</sup> In addition, the contact angles for the NF membranes showed a gradual decrease with increasing interface temperature. In detail, the contact angles were 36.7°, 28.4°, 23.9°, 22.1°, and 19.1° for TFCM@–15, TFCM@5,

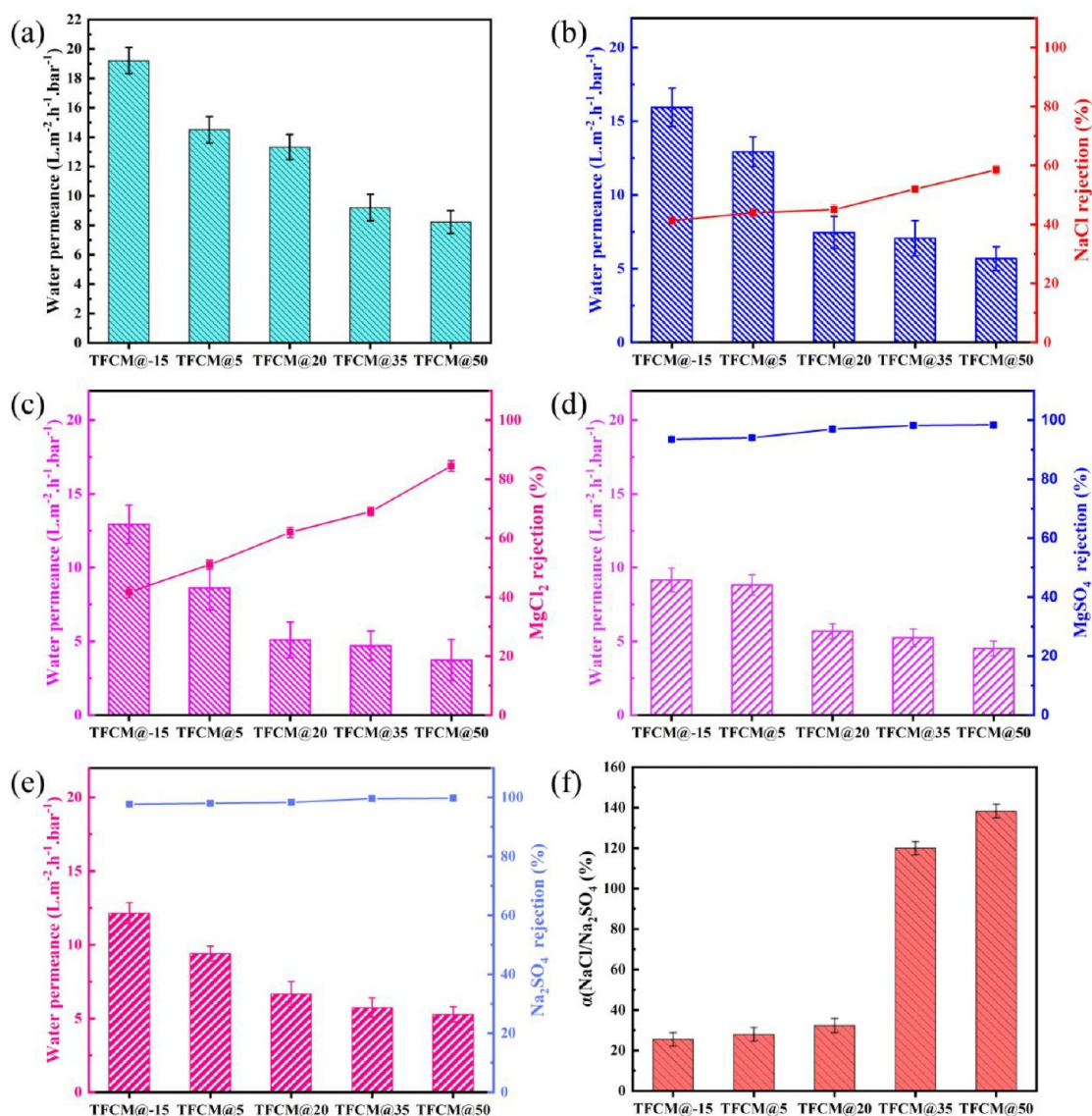


**Figure 6.** (a) Pure water flux, (b) NaCl rejection, (c) MgCl<sub>2</sub> rejection, (d) MgSO<sub>4</sub> rejection, (e) Na<sub>2</sub>SO<sub>4</sub> rejection, and (f) separation factor of NaCl and Na<sub>2</sub>SO<sub>4</sub>.

TFCM@20, TFCM@35, and TFCM@50, respectively. The decreasing water contact angles are indicative of the enhancement for surface hydrophilicity, which can be explained by three aspects. First, the increase in the DNC of the membrane surface led to a decreased content of the hydrophilic  $-\text{COOH}$  groups, as demonstrated by the XPS results. Though the decreased  $-\text{COOH}$  groups would cause a slight increase in the contact angles,<sup>54</sup> the hydrophilic  $-\text{COOH}$  groups still dominated the surface functional groups. Second, the increased interface temperature contributed to a faster IP reaction rate and promoted the self-healing effects of the interfacial reaction.<sup>55</sup> As a result, more unreacted  $-\text{NH}$  groups remained in the interior side of the nascent PA film, thus leading to increased hydrophilicity. Third, the increased surface roughness also facilitated the decrease in contact angles, which has been reported in previous works.<sup>56</sup> Collectively, the TAIP-assisted NF membranes exhibited enhanced hydrophilicity as the interface temperature increased. Figure 5b shows the  $\xi$ -potential of the NF membranes, and a gradual decrease in electronegativity was observed with increasing interface

temperature. The electronegativity of the NF membranes obeyed the sequence TFCM@-15 > TFCM@5 > TFCM@20 > TFCM@35 > TFCM@50. Specifically, the  $\xi$ -potentials were  $-48.4$ ,  $-41.3$ ,  $-34.6$ ,  $-31.4$ , and  $-26.9$  mV at pH 7.0 for TFCM@-15, TFCM@5, TFCM@20, TFCM@35, and TFCM@50, respectively. This result is in accordance with the XPS results, as depicted in Figure 4c, indicating that lower negatively charged  $-\text{COOH}$  groups were obtained when increasing the interface temperature. For a typical negatively charged NF membrane, the surface charge dominated the rejecting behaviors for charged salts and molecules.<sup>57</sup> The changes of the electronegativity would lead to the changes in the separation behavior for the NF membranes to some extent.

As another important parameter, the pore size also dominated the separation behavior for NF membranes via the size exclusion effect.<sup>58</sup> To evaluate the variations of the pore sizes for the NF membranes, the PEGs filtration tests with different molecular weights (200, 400, 600, 800, and 1000 g mol<sup>-1</sup>) were conducted. As revealed in Figure 5c, increasing the interfacial temperature led to a gradual decrease in the

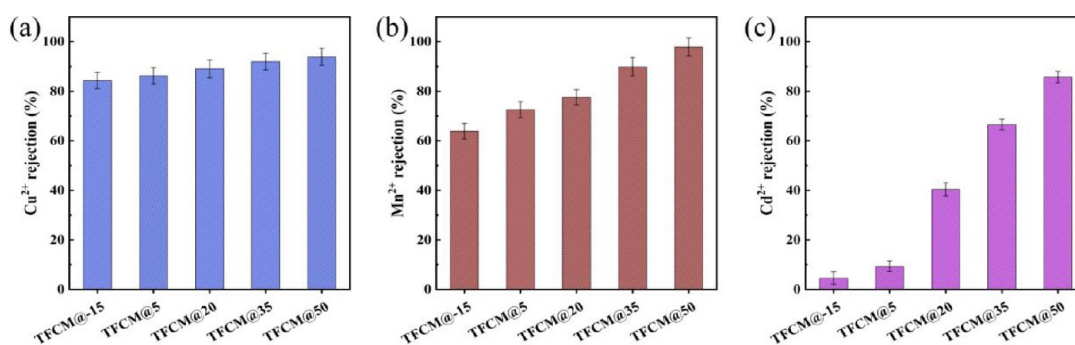


**Figure 7.** Rejection performance of heavy metals for the NF membranes: (a) Cu<sup>2+</sup>, (b) Mn<sup>2+</sup>, and (c) Cd<sup>2+</sup>.

MWCO values for the resultant NF membranes. The MWCOs for TFCM@-15, TFCM@5, TFCM@20, TFCM@35, and TFCM@50 were 430, 400, 385, 375, and 360 Da, respectively. Obviously, the pore diameters of the NF membranes gradually narrowed with increasing interface temperature. The pore size distribution of the NF membranes was further calculated on the basis of the PEG rejections, as shown in Figure 5d. Similar to the PEG-characterized pore size, the position of the characteristic peaks shifted gradually to the left, confirming that a decreased pore size was obtained. In detail, the average pore sizes were 1.07, 1.02, 0.97, 0.94, and 0.91 nm for TFCM@-15, TFCM@5, TFCM@20, TFCM@35, and TFCM@50, respectively (Table S1). The narrowed pore size agrees well with the increased DNC, also confirming that the TAIP strategy contributed to a more cross-linked, dense, and defect-free PA film. In summary, the increased interface temperature resulted in more hydrophilic, lower negatively charged, and narrower pore-sized TFC NF membranes.

**3.4. Filtration Performance of the NF Membranes.** To further evaluate the changes in the separation performance, the permeance and rejection properties of the NF membranes were evaluated. Figure 6a shows the pure water permeance of the NF membranes as a function of the interface temperature, and a gradual decrease in water permeance was observed. Specifically, the water permeance values were  $19.2 \pm 0.1$ ,  $14.5 \pm 0.3$ ,  $13.3 \pm 0.4$ ,  $9.2 \pm 0.3$ , and  $8.2 \pm 0.2$  L m<sup>-2</sup> h<sup>-1</sup> bar<sup>-1</sup> for TFCM@-15, TFCM@5, TFCM@20, TFCM@35, and TFCM@50, respectively. Compared to the TFCM@50 membrane, the water permeance of the TFCM@-15 membrane was two times higher. The decreased water permeance can be ascribed to the thickness and pore diameter of the NF membranes. First, the thickness of the PA film gradually increased with increasing interface temperature, leading to an increase of the transport resistance across the membranes. Consequently, the transport of water molecules through the membranes became harder as the transport resistance increased; thus, a decrease in the water permeance was achieved. In addition, increasing the interface temperature further narrowed the pore sizes of the NF membranes, which is in favor of the confined transport of water molecules.<sup>59</sup> Though the increase in surface roughness and hydrophilicity were helpful for improving the water permeance, the limited enhancement was insufficient to compensate for the flux reduction caused by the thickness and pore size of the PA film. Therefore, the permeance of the NF membranes showed a decrease under the combined effects of pore size, roughness, hydrophilicity, and thickness.

The salt rejections of the resultant NF membranes were investigated by filtering 2000 ppm of NaCl, Na<sub>2</sub>SO<sub>4</sub>, MgCl<sub>2</sub>,

and MgSO<sub>4</sub>. Figure 6b–e depicts the separation behavior of the NF membranes, and an enhanced salt rejection was achieved with increasing interface temperature. In addition, the salt rejection rates for all of the NF membranes were in the order of Na<sub>2</sub>SO<sub>4</sub> > MgSO<sub>4</sub> > MgCl<sub>2</sub> > NaCl, which is consistent with the separation character for typical NF membranes.<sup>34</sup> Specifically, the NaCl rejections for TFCM@-15, TFCM@5, TFCM@20, TFCM@35, and TFCM@50 were 41.3%, 44.0%, 45.0%, 52.0%, and 58.5%, respectively (Figure 6b). As for Na<sub>2</sub>SO<sub>4</sub> rejection, the corresponding values were 97.7%, 98.0%, 98.3%, 99.6%, and 99.7%, respectively (Figure 6e). The enhanced salt rejection of the NF membranes can be assigned to the combined functions of the decreased surface defects, reduced surface charge, and narrowed pore size. First, the increased interface temperature contributed to the fast transport of TMC toward the water/oil interface, leading to a more complete IP reaction and fewer defects being obtained. As a result, the possibility of the salt ions crossing the defect sites within the PA film was greatly reduced. Second, despite the fact that the negative charge of the membrane surface was reduced, the TAIP-assisted NF membrane still exhibited a highly negatively charged potential. In other words, the Donnan exclusion effects between the surface and the charged ions still played an important role. Third, increasing the interface temperature further increased the DNC, and thus, a much smaller pore size was achieved for the TAIP-assisted NF membrane when compared to the bare membrane. The reduced membrane pores can contribute to the rejection of salt ions via enhanced size exclusions. This aspect was likely the main factor for the increased salt rejection for the modified membranes. The separation factor of NaCl to Na<sub>2</sub>SO<sub>4</sub> ( $\alpha$ ), calculated from the rejection of divalent and monovalent salts, also exhibited an obvious improvement (Figure 6f). It can be seen that the separation factor  $\alpha$  increased from 25.5 for TFCM@-15 to 138.3 for TFCM@50. The greatly enhanced selectivity of the NF membranes demonstrated that the TAIP-assisted strategy had great potential in tailoring the performance of the TFC membranes for practical desalination applications.

**3.5. Removal Performance of Heavy Metals.** To further investigate the application potential of the NF membranes for treating wastewater, three model heavy metals (CuCl<sub>2</sub>, MnCl<sub>2</sub>, and CdCl<sub>2</sub>) were employed to evaluate the rejection behavior of the membranes. As shown in Figure 7, the modified NF membranes exhibited an increased rejection for the selected heavy metals. In particular, all of the NF membranes showed relatively high rejections for Cu<sup>2+</sup>, as displayed in Figure 7a. The rejections for Cu<sup>2+</sup> were 84.3%, 86.2%, 89.0%, 91.9%, and 93.9% for TFCM@-15, TFCM@5, TFCM@20, TFCM@35, and TFCM@50,

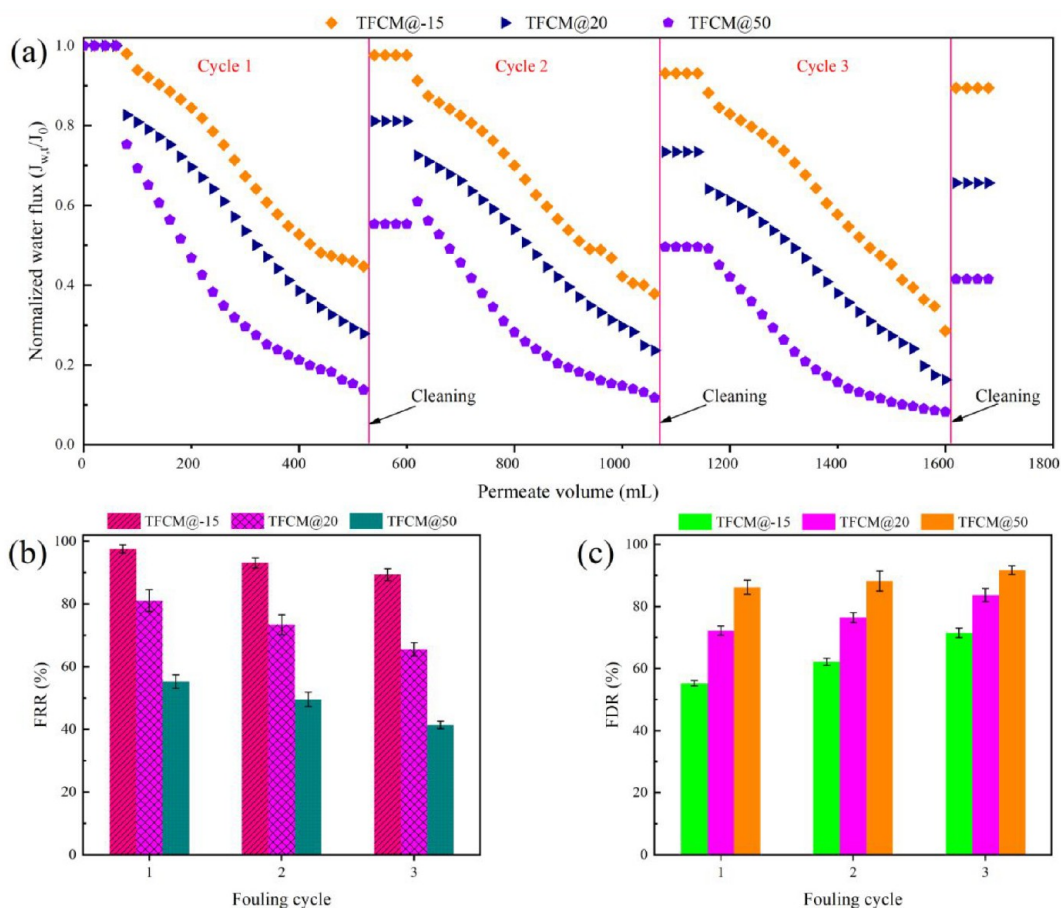


**Figure 8.** Antifouling performance of the NF membranes: (a) normalized water flux during 3 cycles of BSA solutions, (b) FRR, and (c) FDR. Fouling conditions: initial water flux was  $35.0 \text{ L m}^{-2} \text{ h}^{-1}$ , temperature was  $25.0 \pm 0.2 \text{ }^\circ\text{C}$ , and feed solution was composed of 100 ppm BSA and background electrolyte (16 mM NaCl, 1 mM  $\text{NaHCO}_3$ , and 1 mM  $\text{CaCl}_2$ ).

and TFCM@50, respectively. In terms of  $\text{Mn}^{2+}$ , the rejection rate increased from 63.9% for TFCM@-15 to 97.9% for TFCM@50 (Figure 7b). Compared with  $\text{Cu}^{2+}$  and  $\text{Mn}^{2+}$ , the enhancement effect was more obvious for  $\text{Cd}^{2+}$ , as depicted in Figure 7c. For the TFCM@-15 membrane, the rejection rate of  $\text{Cd}^{2+}$  was 4.5%. On increasing the interface temperature from 5 to  $50 \text{ }^\circ\text{C}$ , the  $\text{Cd}^{2+}$  rejection increased from 9.3% for TFCM@5 to 85.7% for TFCM@50. Compared to the TFCM@-15 membrane, the  $\text{Cd}^{2+}$  rejection increased by 62.0% and 81.1% for TFCM@35 and TFCM@50, respectively. Obviously, an NF membrane fabricated at a high interface temperature was more suitable for heavy metal removal. The excellent rejection of heavy metals for the TFCM@50 was also superior to the commercial NF270 membrane, as shown in Figure S6. The differences in rejecting  $\text{Cu}^{2+}$ ,  $\text{Mn}^{2+}$ , and  $\text{Cd}^{2+}$  for the NF membranes can be ascribed to the different hydrated radii and diffusivities.<sup>60–62</sup> Similar to the rejection behavior of four typical salts, the enhanced separation efficiencies for heavy metals of the NF membranes can also be attributed to the reduced negative charge, decreased surface defects, and narrowed pore size. The enhanced heavy metal removal and salt rejection demonstrated that the TAIP-assisted NF membranes had promising applications in both drinking water and wastewater treatment.

**3.6. Antifouling Performance and Stability of the NF Membranes.** The antifouling behavior and stability of the NF membranes play an important role in practical applications.

During the fouling process, TFCM@-15, TFCM@20, and TFCM@50 were chosen for their typical morphological features. Three cycles of fouling tests were conducted using BSA as the model foulant to evaluate the fouling trend of the NF membranes, as shown in Figure 8. A gradual flux decrease was observed for all of the NF membranes, and the antifouling properties were in the order of TFCM@-15 > TFCM@20 > TFCM@50 (Figure 8a). The FRR values for all of the NF membranes exhibited a decrease with increasing fouling cycles (Figure 8b), indicating that the irreversible fouling accumulated gradually on the membrane surfaces. Specifically, the FRR decreased from 97.6 to 89.4, from 81.1 to 65.6, and from 55.3 to 41.5 for TFCM@-15, TFCM@20, and TFCM@50, respectively. On the contrary, a gradual increase in the FDR was obtained for all of the NF membranes (Figure 8c), confirming that more serious fouling occurred with the extension of fouling cycles. As the TFCM@20 membrane was fabricated at room temperature, its surface morphology was close to that of commercial NF membranes. Therefore, TFCM@-15 was expected to have better antifouling properties than traditional nodular-like NF membranes. Both the FRR and the FDR values demonstrated that the best antifouling performance belonged to the TFCM@-15 membrane possessing the smoothest surface, whereas the TFCM@50 membranes featuring coffee-ring-like morphologies exhibited the most serious fouling. Three aspects could be attributed to the excellent antifouling behavior of TFCM@-

15. First, the smooth surface was not beneficial for the deposition of the foulant, whereas the irregular surfaces tended to trap foulants during filtration; Second, a lower operation pressure was needed for TFCM@-15 when reaching the same initial water flux, thus forming a relatively loose cake layer that could be easily removed under hydraulic cleaning; Third, the enhanced electrostatic repulsion between the negatively charged membrane surface and the BSA reduced the deposition of foulants, favoring less fouling of TFCM@-15. The three types of NF membranes presented stable water permeance and  $\text{Na}_2\text{SO}_4$  rejection during a 40 h operation test, demonstrating that the TAIP-assisted NF membranes had outstanding and comparable performance stability in long-term filtrations (Figure S7). Notably, although a superior antifouling performance was achieved for the NF membranes with smooth surfaces, physical cleaning was insufficient to remove the irreversible fouling during long-term operation. To maintain the high separation efficiency of the NF membranes, suitable pretreatment technologies and/or highly efficient chemical cleaning strategies still need to be integrated with NF-based separation processes. In summary, the TAIP strategy not only efficiently regulates the antifouling behavior but also tailors the morphology and separation performance of the NF membranes, showing it is a promising method for in situ modulating TFC desalination membranes.

#### 4. CONCLUSIONS

In conclusion, a novel TAIP strategy was employed to facilitate, efficiently, and feasibly tailor the surface morphologies and separation performance of the TFC NF membranes. This method was realized via controlling the temperature of the oil phase, thus confining the diffusion rate of the PIP and TMC monomers and the performance of the fabricated NF membranes. The morphological, structural, and separation behaviors of the resultant NF membranes were systematically evaluated. A low interface temperature promoted the generation of an ultrathin and smooth PA film featuring high water permeance, high salt rejection, and excellent antifouling properties. On the contrary, the NF membranes fabricated at a high interface temperature exhibited a rough, dense, and thick PA film possessing moderate water permeance, excellent salt rejection, and heavy metal removal efficiency. The enhanced separation efficiencies of the TAIP-assisted NF membranes are ascribed to the greatly increased membrane integrity and DNC. Interestingly, the TFCM@50 membrane exhibited a special coffee-ring-like morphology, which was likely caused by the temperature-induced interface instability. These results confirm that the surface morphologies, separation features, and fouling behaviors of the TFC NF membranes could be accurately regulated by the TAIP strategy. Considering the excellent separation efficiencies and operational feasibility, the TAIP strategy has great promise in regulating the performance of the TFC membranes for practical environmental applications.

#### ■ ASSOCIATED CONTENT

##### SI Supporting Information

The Supporting Information is available free of charge at <https://pubs.acs.org/doi/10.1021/acsami.1c17783>.

Calculation of the cross-linking degree; interfacial polymerization process of PIP and TMC; schematic illustration of the testing device for the NF performance

evaluation; SEM image of the PES support; TEM images of the membranes; high-resolution XPS spectra of the C 1s and N 1s elements; removal of heavy metals for NF270; stability of the NF membranes during a 40 h long-term operation; MWCO,  $\mu_p$ , and  $\delta$  of the NF membranes; performance comparison of TFCM@-15 with commercial NF and the state-of-art NF membranes reported in the literature (PDF)

#### ■ AUTHOR INFORMATION

##### Corresponding Author

Xuewu Zhu – School of Municipal and Environmental Engineering, Shandong Jianzhu University, Jinan 250101, China; [orcid.org/0000-0003-2939-3111](https://orcid.org/0000-0003-2939-3111); Phone: +86 053186367291; Email: [zhuxuewu1314@163.com](mailto:zhuxuewu1314@163.com); Fax: +86 053186367291

##### Authors

Xiaoxiang Cheng – School of Municipal and Environmental Engineering, Shandong Jianzhu University, Jinan 250101, China

Cunxian Lai – School of Municipal and Environmental Engineering, Shandong Jianzhu University, Jinan 250101, China

Jinyu Li – School of Municipal and Environmental Engineering, Shandong Jianzhu University, Jinan 250101, China

Weiwei Zhou – Shandong Urban Construction Vocational College, Jinan 250103, China

Zihui Wang – State Key Laboratory of Urban Water Resource and Environment, School of Environment, Harbin Institute of Technology, Harbin 150090, China

Junwen Ding – State Key Laboratory of Urban Water Resource and Environment, School of Environment, Harbin Institute of Technology, Harbin 150090, China

Xinyu Zhang – School of Municipal and Environmental Engineering, Shandong Jianzhu University, Jinan 250101, China

Daoji Wu – School of Municipal and Environmental Engineering, Shandong Jianzhu University, Jinan 250101, China

Heng Liang – State Key Laboratory of Urban Water Resource and Environment, School of Environment, Harbin Institute of Technology, Harbin 150090, China; [orcid.org/0000-0002-9100-6007](https://orcid.org/0000-0002-9100-6007)

Congcong Zhao – College of Geography and Environment, Shandong Normal University, Jinan 250014, China

Complete contact information is available at: <https://pubs.acs.org/doi/10.1021/acsami.1c17783>

##### Notes

The authors declare no competing financial interest.

#### ■ ACKNOWLEDGMENTS

This research was jointly supported by the Scientific Research Leader Studio of Jinan (2019CXRC065), the Shandong Provincial Major Scientific and Technological Innovation Project (MSTIP) (2020CXGC011203), the National Natural Science Foundation of China (51908334, 22008162), and the China Postdoctoral Science Foundation (2020T130383).

## REFERENCES

- (1) Li, Q.; Liao, Z.; Fang, X.; Xie, J.; Ni, L.; Wang, D.; Qi, J.; Sun, X.; Wang, L.; Li, J. Tannic Acid Assisted Interfacial Polymerization Based Loose Thin-Film Composite NF Membrane for Dye/Salt Separation. *Desalination* **2020**, *479*, 114343.
- (2) Zhou, D.; Zhu, L.; Fu, Y.; Zhu, M.; Xue, L. Development of Lower Cost Seawater Desalination Processes Using Nanofiltration Technologies — a Review. *Desalination* **2015**, *376*, 109–116.
- (3) Cheng, X.; Liang, H.; Ding, A.; Zhu, X.; Tang, X.; Gan, Z.; Xing, J.; Wu, D.; Li, G. Application of Fe(II)/Peroxymonosulfate for Improving Ultrafiltration Membrane Performance in Surface Water Treatment: Comparison with Coagulation and Ozonation. *Water Res.* **2017**, *124*, 298–307.
- (4) Cheng, X.; Wu, D.; Liang, H.; Zhu, X.; Tang, X.; Gan, Z.; Xing, J.; Luo, X.; Li, G. Effect of Sulfate Radical-Based Oxidation Pretreatments for Mitigating Ceramic UF Membrane Fouling Caused by Algal Extracellular Organic Matter. *Water Res.* **2018**, *145*, 39–49.
- (5) Cheng, X.; Zhou, W.; Wu, D.; Luo, C.; Jia, R.; Li, P.; Zheng, L.; Zhu, X.; Liang, H. Pre-Deposition Layers for Alleviating Ultrafiltration Membrane Fouling by Organic Matter: Role of Hexagonally and Cubically Ordered Mesoporous Carbons. *Sep. Purif. Technol.* **2020**, *240*, 116599.
- (6) Han, Y.; Xu, Z.; Gao, C. Ultrathin Graphene Nanofiltration Membrane for Water Purification. *Adv. Funct. Mater.* **2013**, *23*, 3693–3700.
- (7) Xu, X. L.; Lin, F. W.; Du, Y.; Zhang, X.; Wu, J.; Xu, Z. K. Graphene Oxide Nanofiltration Membranes Stabilized by Cationic Porphyrin for High Salt Rejection. *ACS Appl. Mater. Interfaces* **2016**, *8*, 12588–12593.
- (8) Zhu, X.; Cheng, X.; Luo, X.; Liu, Y.; Xu, D.; Tang, X.; Gan, Z.; Yang, L.; Li, G.; Liang, H. Ultrathin Thin-Film Composite Polyamide Membranes Constructed on Hydrophilic Poly(vinyl alcohol) Decorated Support toward Enhanced Nanofiltration Performance. *Environ. Sci. Technol.* **2020**, *54*, 6365–6374.
- (9) Lim, Y. J.; Goh, K.; Kurihara, M.; Wang, R. Seawater Desalination by Reverse Osmosis: Current Development and Future Challenges in Membrane Fabrication — a Review. *J. Membr. Sci.* **2021**, *629*, 119292.
- (10) Pendergast, M. M.; Hoek, E. M. V. A Review of Water Treatment Membrane Nanotechnologies. *Energy Environ. Sci.* **2011**, *4*, 1946–1971.
- (11) Zhao, Y.; Tong, T.; Wang, X.; Lin, S.; Reid, E. M.; Chen, Y. Differentiating Solutes with Precise Nanofiltration for Next Generation Environmental Separations: A Review. *Environ. Sci. Technol.* **2021**, *55*, 1359–1376.
- (12) Zhu, X.; Yang, Z.; Gan, Z.; Cheng, X.; Tang, X.; Luo, X.; Xu, D.; Li, G.; Liang, H. Toward Tailoring Nanofiltration Performance of Thin-Film Composite Membranes: Novel Insights into the Role of Poly(vinyl alcohol) Coating Positions. *J. Membr. Sci.* **2020**, *614*, 118526.
- (13) Liu, F.; Wang, L.; Li, D.; Liu, Q.; Deng, B. A Review: The Effect of the Microporous Support During Interfacial Polymerization on the Morphology and Performances of a Thin Film Composite Membrane for Liquid Purification. *RSC Adv.* **2019**, *9*, 35417–35428.
- (14) Ismail, A. F.; Padaki, M.; Hilal, N.; Matsuura, T.; Lau, W. J. Thin Film Composite Membrane — Recent Development and Future Potential. *Desalination* **2015**, *356*, 140–148.
- (15) Raaijmakers, M. J. T.; Benes, N. E. Current Trends in Interfacial Polymerization Chemistry. *Prog. Polym. Sci.* **2016**, *63*, 86–142.
- (16) Xu, D.; Zhu, X.; Luo, X.; Guo, Y.; Liu, Y.; Yang, L.; Tang, X.; Li, G.; Liang, H. MXene Nanosheet Templated Nanofiltration Membranes toward Ultrahigh Water Transport. *Environ. Sci. Technol.* **2021**, *55*, 1270–1278.
- (17) Zhu, X.; Liang, H.; Tang, X.; Bai, L.; Zhang, X.; Gan, Z.; Cheng, X.; Luo, X.; Xu, D.; Li, G. Supramolecular-Based Regenerable Coating Layer of a Thin-Film Composite Nanofiltration Membrane for Simultaneously Enhanced Desalination and Antifouling Properties. *ACS Appl. Mater. Interfaces* **2019**, *11*, 21137–21149.
- (18) Freger, V.; Ramon, G. Z. Polyamide Desalination Membranes: Formation, Structure, and Properties. *Prog. Polym. Sci.* **2021**, *122*, 101451.
- (19) Lau, W.-J.; Lai, G.-S.; Li, J.; Gray, S.; Hu, Y.; Misdan, N.; Goh, P.-S.; Matsuura, T.; Azelee, I. W.; Ismail, A. F. Development of Microporous Substrates of Polyamide Thin Film Composite Membranes for Pressure-Driven and Osmotically-Driven Membrane Processes: A Review. *J. Ind. Eng. Chem.* **2019**, *77*, 25–59.
- (20) Ghosh, A. K.; Hoek, E. M. V. Impacts of Support Membrane Structure and Chemistry on Polyamide–Polysulfone Interfacial Composite Membranes. *J. Membr. Sci.* **2009**, *336*, 140–148.
- (21) Li, X.; Li, Q.; Fang, W.; Wang, R.; Krantz, W. B. Effects of the Support on the Characteristics and Permselectivity of Thin Film Composite Membranes. *J. Membr. Sci.* **2019**, *580*, 12–23.
- (22) Dai, R.; Li, J.; Wang, Z. Constructing Interlayer to Tailor Structure and Performance of Thin-Film Composite Polyamide Membranes: A Review. *Adv. Colloid Interface Sci.* **2020**, *282*, 102204.
- (23) Yang, Z.; Sun, P.-F.; Li, X.; Gan, B.; Wang, L.; Song, X.; Park, H.-D.; Tang, C. Y. A Critical Review on Thin-Film Nanocomposite Membranes with Interlayered Structure: Mechanisms, Recent Developments, and Environmental Applications. *Environ. Sci. Technol.* **2020**, *54*, 15563–15583.
- (24) Zhang, R.; Tian, J.; Gao, S.; Van der Bruggen, B. How to Coordinate the Trade-Off between Water Permeability and Salt Rejection in Nanofiltration? *J. Mater. Chem. A* **2020**, *8*, 8831–8847.
- (25) Zhu, X.; Zhang, X.; Li, J.; Luo, X.; Xu, D.; Wu, D.; Wang, W.; Cheng, X.; Li, G.; Liang, H. Crumple-Textured Polyamide Membranes via MXene Nanosheet-Regulated Interfacial Polymerization for Enhanced Nanofiltration Performance. *J. Membr. Sci.* **2021**, *635*, 119536.
- (26) Zhang, X.; Chen, T.-H.; Chen, F.-F.; Wu, H.; Yu, C.-Y.; Liu, L.-F.; Gao, C.-J. Structure Adjustment for Enhancing the Water Permeability and Separation Selectivity of the Thin Film Composite Nanofiltration Membrane Based on a Dendritic Hyperbranched Polymer. *J. Membr. Sci.* **2021**, *618*, 118455.
- (27) Zhu, C.-Y.; Liu, C.; Yang, J.; Guo, B.-B.; Li, H.-N.; Xu, Z.-K. Polyamide Nanofilms with Linearly-Tunable Thickness for High Performance Nanofiltration. *J. Membr. Sci.* **2021**, *627*, 119142.
- (28) Tan, Z.; Chen, S.; Peng, X.; Zhang, L.; Gao, C. Polyamide Membranes with Nanoscale Turing Structures for Water Purification. *Science* **2018**, *360*, 518–521.
- (29) Shen, K.; Li, P.; Zhang, T.; Wang, X. Salt-Tuned Fabrication of Novel Polyamide Composite Nanofiltration Membranes with Three-Dimensional Turing Structures for Effective Desalination. *J. Membr. Sci.* **2020**, *607*, 118153.
- (30) Khorshidi, B.; Thundat, T.; Fleck, B. A.; Sadzadeh, M. A Novel Approach toward Fabrication of High Performance Thin Film Composite Polyamide Membranes. *Sci. Rep.* **2016**, *6*, 22069.
- (31) Liu, C.; Wang, W.; Zhu, L.; Cui, F.; Xie, C.; Chen, X.; Li, N. High-Performance Nanofiltration Membrane with Structurally Controlled PES Substrate Containing Electrically Aligned CNTs. *J. Membr. Sci.* **2020**, *605*, 118104.
- (32) Shang, W.; Sun, F.; Jia, W.; Guo, J.; Yin, S.; Wong, P. W.; An, A. K. High-Performance Nanofiltration Membrane Structured with Enhanced Stripe Nano-Morphology. *J. Membr. Sci.* **2020**, *600*, 117852.
- (33) Yan, F.; Chen, H.; Lü, Y.; Lü, Z.; Yu, S.; Liu, M.; Gao, C. Improving the Water Permeability and Antifouling Property of Thin-Film Composite Polyamide Nanofiltration Membrane by Modifying the Active Layer with Triethanolamine. *J. Membr. Sci.* **2016**, *513*, 108–116.
- (34) Zhu, X.; Xu, D.; Gan, Z.; Luo, X.; Tang, X.; Cheng, X.; Bai, L.; Li, G.; Liang, H. Improving Chlorine Resistance and Separation Performance of Thin-Film Composite Nanofiltration Membranes with In-Situ Grafted Melamine. *Desalination* **2020**, *489*, 114539.
- (35) Zhu, X.; Tang, X.; Luo, X.; Cheng, X.; Xu, D.; Gan, Z.; Wang, W.; Bai, L.; Li, G.; Liang, H. Toward Enhancing the Separation and Antifouling Performance of Thin-Film Composite Nanofiltration

- Membranes: A Novel Carbonate-Based Preoccupation Strategy. *J. Colloid Interface Sci.* **2020**, *571*, 155–165.
- (36) Zhu, X.; Tang, X.; Luo, X.; Yang, Z.; Cheng, X.; Gan, Z.; Xu, D.; Li, G.; Liang, H. Stainless Steel Mesh Supported Thin-Film Composite Nanofiltration Membranes for Enhanced Permeability and Regeneration Potential. *J. Membr. Sci.* **2021**, *618*, 118738.
- (37) Xia, D.; Zhang, M.; Tong, C.; Wang, Z.; Liu, H.; Zhu, L. In-Situ Incorporating Zwitterionic Nanocellulose into Polyamide Nanofiltration Membrane Towards Excellent Perm-Selectivity and Antifouling Performances. *Desalination* **2022**, *521*, 115397.
- (38) Qiu, Z.-L.; Fang, L.-F.; Shen, Y.-J.; Yu, W.-H.; Zhu, B.-K.; Hélix-Nielsen, C.; Zhang, W. Ionic Dendrimer Based Polyamide Membranes for Ion Separation. *ACS Nano* **2021**, *15*, 7522–7535.
- (39) Song, X.; Gan, B.; Yang, Z.; Tang, C. Y.; Gao, C. Confined Nanobubbles Shape the Surface Roughness Structures of Thin Film Composite Polyamide Desalination Membranes. *J. Membr. Sci.* **2019**, *582*, 342–349.
- (40) Wang, J.; Xu, R.; Yang, F.; Kang, J.; Cao, Y.; Xiang, M. Probing Influences of Support Layer on the Morphology of Polyamide Selective Layer of Thin Film Composite Membrane. *J. Membr. Sci.* **2018**, *556*, 374–383.
- (41) Peng, L. E.; Yao, Z.; Liu, X.; Deng, B.; Guo, H.; Tang, C. Y. Tailoring Polyamide Rejection Layer with Aqueous Carbonate Chemistry for Enhanced Membrane Separation: Mechanistic Insights, Chemistry-Structure-Property Relationship, and Environmental Implications. *Environ. Sci. Technol.* **2019**, *53*, 9764–9770.
- (42) Ma, X.-H.; Yao, Z.-K.; Yang, Z.; Guo, H.; Xu, Z.-L.; Tang, C. Y.; Elimelech, M. Nanofoaming of Polyamide Desalination Membranes to Tune Permeability and Selectivity. *Environ. Sci. Technol. Lett.* **2018**, *5*, 123–130.
- (43) Yang, Z.; Zhou, Z.-w.; Guo, H.; Yao, Z.; Ma, X.-h.; Song, X.; Feng, S.-P.; Tang, C. Y. Tannic Acid/Fe<sup>3+</sup> Nanoscaffold for Interfacial Polymerization: Toward Enhanced Nanofiltration Performance. *Environ. Sci. Technol.* **2018**, *52*, 9341–9349.
- (44) Jin, Y.; Su, Z. Effects of Polymerization Conditions on Hydrophilic Groups in Aromatic Polyamide Thin Films. *J. Membr. Sci.* **2009**, *330*, 175–179.
- (45) Tian, J.; Chang, H.; Gao, S.; Zong, Y.; Van der Bruggen, B.; Zhang, R. Direct Generation of an Ultrathin (8.5 nm) Polyamide Film with Ultrahigh Water Permeance via In-Situ Interfacial Polymerization on Commercial Substrate Membrane. *J. Membr. Sci.* **2021**, *634*, 119450.
- (46) Zhai, Z.; Zhao, N.; Liu, J.; Dong, W.; Li, P.; Sun, H.; Jason Niu, Q. Advanced Nanofiltration Membrane Fabricated on the Porous Organic Cage Tailored Support for Water Purification Application. *Sep. Purif. Technol.* **2020**, *230*, 115845.
- (47) Han, S.; Wang, Z.; Cong, S.; Zhu, J.; Zhang, X.; Zhang, Y. Root-Like Polyamide Membranes with Fast Water Transport for High-Performance Nanofiltration. *J. Mater. Chem. A* **2020**, *8*, 25028–25034.
- (48) Wang, J.-J.; Yang, H.-C.; Wu, M.-B.; Zhang, X.; Xu, Z.-K. Nanofiltration Membranes with Cellulose Nanocrystals as an Interlayer for Unprecedented Performance. *J. Mater. Chem. A* **2017**, *5*, 16289–16295.
- (49) Dai, R.; Han, H.; Wang, T.; Li, X.; Wang, Z. Enhanced Removal of Hydrophobic Endocrine Disrupting Compounds from Wastewater by Nanofiltration Membranes Intercalated with Hydrophilic MoS<sub>2</sub> Nanosheets: Role of Surface Properties and Internal Nanochannels. *J. Membr. Sci.* **2021**, *628*, 119267.
- (50) Gui, L.; Dong, J.; Fang, W.; Zhang, S.; Zhou, K.; Zhu, Y.; Zhang, Y.; Jin, J. Ultrafast Ion Sieving from Honeycomb-Like Polyamide Membranes Formed Using Porous Protein Assemblies. *Nano Lett.* **2020**, *20*, 5821–5829.
- (51) Guo, H.; Yao, Z.; Yang, Z.; Ma, X.; Wang, J.; Tang, C. Y. A One-Step Rapid Assembly of Thin Film Coating Using Green Coordination Complexes for Enhanced Removal of Trace Organic Contaminants by Membranes. *Environ. Sci. Technol.* **2017**, *51*, 12638–12643.
- (52) Gao, S.; Zhu, Y.; Gong, Y.; Wang, Z.; Fang, W.; Jin, J. Ultrathin Polyamide Nanofiltration Membrane Fabricated on Brush-Painted Single-Walled Carbon Nanotube Network Support for Ion Sieving. *ACS Nano* **2019**, *13*, 5278–5290.
- (53) Liu, Y.-l.; Zhao, Y.-y.; Wang, X.-m.; Wen, X.-h.; Huang, X.; Xie, Y. F. Effect of Varying Piperazine Concentration and Post-Modification on Prepared Nanofiltration Membranes in Selectively Rejecting Organic Micropollutants and Salts. *J. Membr. Sci.* **2019**, *582*, 274–283.
- (54) Zhu, J.; Hou, J.; Yuan, S.; Zhao, Y.; Li, Y.; Zhang, R.; Tian, M.; Li, J.; Wang, J.; Van der Bruggen, B. MOF-Positioned Polyamide Membranes with a Fishnet-Like Structure for Elevated Nanofiltration Performance. *J. Mater. Chem. A* **2019**, *7*, 16313–16322.
- (55) Zhu, J.; Hou, J.; Zhang, R.; Yuan, S.; Li, J.; Tian, M.; Wang, P.; Zhang, Y.; Volodin, A.; Van der Bruggen, B. Rapid Water Transport through Controllable, Ultrathin Polyamide Nanofilms for High-Performance Nanofiltration. *J. Mater. Chem. A* **2018**, *6*, 15701–15709.
- (56) Wang, J.; Zhu, J.; Zhang, Y.; Liu, J.; Van der Bruggen, B. Nanoscale Tailor-Made Membranes for Precise and Rapid Molecular Sieve Separation. *Nanoscale* **2017**, *9*, 2942–2957.
- (57) Zhang, H.; He, Q.; Luo, J.; Wan, Y.; Darling, S. B. Sharpening Nanofiltration: Strategies for Enhanced Membrane Selectivity. *ACS Appl. Mater. Interfaces* **2020**, *12*, 39948–39966.
- (58) Cheng, X.; Qin, Y.; Ye, Y.; Chen, X.; Wang, K.; Zhang, Y.; Figoli, A.; Drioli, E. Finely Tailored Pore Structure of Polyamide Nanofiltration Membranes for Highly-Efficient Application in Water Treatment. *Chem. Eng. J.* **2021**, *417*, 127976.
- (59) Zhang, Z.; Shi, X.; Wang, R.; Xiao, A.; Wang, Y. Ultra-Permeable Polyamide Membranes Harvested by Covalent Organic Framework Nanofiber Scaffolds: A Two-in-One Strategy. *Chem. Sci.* **2019**, *10*, 9077–9083.
- (60) Tansel, B.; Sager, J.; Rector, T.; Garland, J.; Strayer, R. F.; Levine, L.; Roberts, M.; Hummerick, M.; Bauer, J. Significance of Hydrated Radius and Hydration Shells on Ionic Permeability During Nanofiltration in Dead End and Cross Flow Modes. *Sep. Purif. Technol.* **2006**, *51*, 40–47.
- (61) Tian, J.; Chang, H.; Gao, S.; Zhang, R. How to Fabricate a Negatively Charged NF Membrane for Heavy Metal Removal Via the Interfacial Polymerization between PIP and TMC? *Desalination* **2020**, *491*, 114499.
- (62) Zhu, W.-P.; Gao, J.; Sun, S.-P.; Zhang, S.; Chung, T.-S. Poly(amidoamine) Dendrimer (PAMAM) Grafted on Thin Film Composite (TFC) Nanofiltration (NF) Hollow Fiber Membranes for Heavy Metal Removal. *J. Membr. Sci.* **2015**, *487*, 117–126.

## NOTE ADDED AFTER ASAP PUBLICATION

This paper was published ASAP on November 24, 2021. Congcong Zhao was added as an additional co-author on the paper, the corrected version was reposted on November 24, 2021.